Journal of Colloid and Interface Science 677 (2025) 231–243

Contents lists available at ScienceDirect

Journal of Colloid And Interface Science

journal homepage: www.elsevier.com/locate/jcis

Regular Article

Intrinsic dynamics of emulsions: Experiments in microgravity on the International Space Station

V. Lorusso [a,1], D. Orsi [a,1], M. Vaccari [a], F. Ravera [b], E. Santini [b], A.P. Chondrou [c], M. Kostoglou [c], T.D. Karapantsios [c], R. McMillin [d], J.K. Ferri [d], S. Vincent-Bonnieu [e], L. Liggieri [b], L. Cristofolini [a,*]

[a] Department of Mathematics, Physics and Computer Sciences, University of Parma, 43123 Parma, Italy
[b] CNR- Institute of Condensed Matter Chemistry and Technologies for Energy, Unit of Genova, 16149 Genova, Italy
[c] Department of Chemical Technology and Industrial Chemistry, School of Chemistry, Aristotle University of Thessaloniki, Thessaloniki 54124, Greece
[d] Department of Chemical and Life Science Engineering, College of Engineering, Virginia Commonwealth University, Richmond, VA 23220, United States
[e] ESA/ESTEC, European Space Research and Technology Centre, Keplerlaan 1, 2201 AZ Noordwijk, the Netherlands

GRAPHICAL ABSTRACT

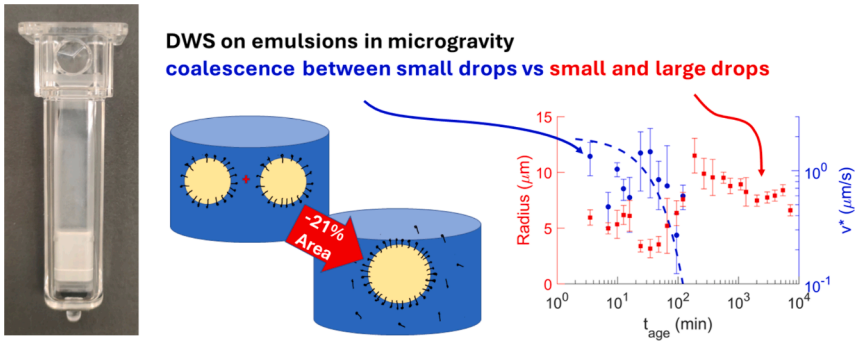

ARTICLE INFO

Keywords:
Emulsions
Microgravity
Diffusing Wave Spectroscopy (DWS)
Optical Monte Carlo simulations

ABSTRACT

Hypothesis: In order to understand the basic mechanisms affecting emulsion stability, the intrinsic dynamics of the drop population must be investigated. We hypothesize that transient ballistic motion can serve as a marker of interactions between drops. In 1G conditions, buoyancy-induced drop motion obscures these interactions. The microgravity condition onboard the International Space Station enable this investigation.

Abbreviations: APD, avalanche photodiode; BS, backscattering geometry, referred to DWS light collection; C12EO21, non-ionic surfactant 21-ethylene glycol mono *n*-dodecyl ether, CAS 9002-92-0; CF, correlation function; CMC, critical micelle concentration; DLS, dynamic light scattering; DSD, drop size distribution; DWS, diffusing wave spectroscopy; ESA, European Space Agency; FW, forward geometry, referred to DWS light collection; HLB, hydrophile/lipophile balance; ISS, International Space Station; IT, interface tension; MCT, medium chain triglyceride, CAS 73398-61-5; MSD, mean square displacement; NP, nanoparticle; PDF, probability density function; SC, sample cell; SCU, sample cell unit; SMD, soft matter dynamics (the instrument onboard ISS); XPCS, X-ray photon correlation spectroscopy; 1G, normal gravity conditions.

* Corresponding author.
E-mail address: luigi.cristofolini@unipr.it (L. Cristofolini).
[1] Equal Contribution.

https://doi.org/10.1016/j.jcis.2024.07.205
Received 10 April 2024; Received in revised form 23 July 2024; Accepted 25 July 2024
Available online 26 July 2024

Soft matter dynamics
Dynamic transition
Drop size distribution
Coalescence/aggregation
Non-ionic surfactants
Ballistic motion
Brownian dynamics

Experiments: We performed Diffusing Wave Spectroscopy (DWS) experiments in the ESA Soft Matter Dynamics (SMD) facility. We used Monte Carlo simulations of photon trajectory to support data analysis. The analysis framework was validated by ground-based characterizations of the initial drop size distribution (DSD) and the properties of the oil/water interface in the presence of surfactant.
Findings: We characterized the drop size distribution and found to be bi-disperse. Drop dynamics shows transient ballistic features at early times, reaching a stationary regime of primarily diffusion-dominated motion. This suggests different ageing mechanisms: immediately after emulsification, the main mechanism is coalescence or aggregation between small drops. However at later times, ageing proceeds via coalescence or aggregation of small with large drops in some emulsions. Our results elucidate new processes relevant to emulsion stability with potential impact on industrial processes on Earth, as well as enabling technologies for space exploration.

1. Introduction

1.1. Emulsions

Emulsions are colloidal dispersions of two or more immiscible liquids. Emulsions are central in a large number of processes and products – from food and pharma to oil industry, paints, lubrication and detergency – where effective methodologies are required either for their stabilisation or destabilisation.

Several classes of synthetic surfactant molecules are utilised as stabilisers (or destabilisers) in emulsion technologies. In the current art, surfactants are often utilised in large excess quantities, raising concerns around environment, sustainability, and governance. In this respect, an important trend is to replace ionic surfactants with non-ionic surfactants, as well as seeking to reduce or optimize the amount of surfactant used.

Though the fundamental knowledge on processes and principles underlying the formation and stability of emulsions has made important progresses during the last decades, the application to practical formulation still relies on semiempirical concepts, such as the Hydrophile / Lipophile Balance (HLB) [1]. The HLB framework and its refinements, such as the Hydrophilic-Lipophilic Deviation (HLD) approach [2,3], can be useful to address the formulation in terms of surfactants suitable for given applications, but do not allow optimising the amounts of surfactants. The packing parameter concepts [4,5] are instead based on well-defined geometrical and steric properties of the surfactant molecules. However, by definition, this approach describes situations of saturated surfactant assembling, which is useful to predict the final fate of an emulsion but finds little application when targeting the kinetic stabilisation of regular emulsions formulated with optimized surfactant quantities, for example, using concentrations below the Critical Micelle Concentration (CMC).

Furthermore, the process of emulsification often requires much more energy than what is embedded in the final product; most of the energy employed is dissipated via viscous heating. Drop coalescence may occur during and immediately after emulsification also depending on the interfacial properties [6]. Therefore, a better understanding of drop-drop interactions is expected to lead to more efficient emulsification techniques, resulting in a more rational use of energy.

To pursue a design basis elaborating a more rationale use of resources in emulsion technology, a more fundamental understanding of the emulsion evolution, from its formation to the final state of kinetic stability is needed. Since kinetic stability depends on drop dynamics, a fundamental understanding of the macroscopic properties of population dynamic and drop interactions is needed. Typically, key performance indicators are described in terms of statistical indicators, such as mean drop size, the drop size distribution (DSD), and by the types of dynamics displayed in these populations.

Macroemulsions are thermodynamically unstable systems due to the large interfacial area of droplets. These emulsions therefore evolve towards a minimal interfacial area based on drop interaction mechanisms by increasing the average drop size and reducing the free energy. Among these mechanisms the most important are aggregation [7,8], either reversible or irreversible, coalescence [9] and Ostwald Ripening [10], as shown in Fig. 1. In Earth-based (1G) conditions, these dynamics are convoluted with gravity-driven process such creaming and sedimentation. Coalescence is related to the stability of the liquid film between drops. Hydrodynamic and mechanical interactions at the interface can cause the thinning of this film, possibly leading to its rupture and to drop merging. Alternatively, a stable film may form, and in this case aggregation occurs.

Ostwald ripening is driven by the difference in the Laplace pressure between small and large drops. Laplace pressure is in fact inversely proportional to the drop radius. Provided the dispersed phase is soluble in the continuous phase, this pressure difference drives a net mass transfer which makes larger drops grow, or “ripen”, at the expenses of the small ones, shifting the DSD towards larger sizes [10]. After affecting the interfacial properties of droplets, surfactants can be properly utilised [6,11] to hinder their aggregation [12,13] and coalescence [14,15] or to influence Ostwald ripening [16,17].

Despite the extensive literature on the stability of emulsions, and the recent progresses in the investigation of de-emulsification phenomena [18], the topic is far from being fully understood.

Although creaming and/or sedimentation can be mitigated by matching the density between dispersed and continuous phases, this approach severely limits the selection of dispersed and continuous phases which in turn limits the physicochemical relevance of the subject systems to application [19]. A complete understanding of these fundamental mechanisms can therefore benefit from investigations performed under microgravity conditions. With this aim, we have performed the emulsion aging experiments onboard the International Space Station. In microgravity conditions, we anticipate drop dynamics to be governed solely by Brownian motion and surface forces.

1.2. Diffusing Wave Spectroscopy

Diffusing Wave Spectroscopy (DWS)[20–23] is an ideal technique for non-invasive investigation of emulsions, as well as of other turbid disordered systems like colloidal suspensions and foams [24–33]. DWS is a correlation spectroscopy, i.e., it operates in the time domain. The analysis of the time correlation fluctuations of partially coherent light multiply scattered in the sample yields information on microscopic relative displacements of the scattering centres, easily reaching sub-nanometric sensitivity. DWS probes the bulk of the sample, as opposed to optical techniques accessing the regions of the sample closer to the container walls, where dynamics and ageing processes are influenced by the confining geometry.

These advantages are offset by a certain degree of difficulty in the DWS data interpretation as compared to other correlation spectroscopy techniques such as Dynamic Light Scattering; a detailed analysis is required to extract the physical parameters from the measured intensity autocorrelation functions. Light is detected after many scattering events, and interference between light beams following multiple paths results in a speckle pattern, whose dynamics reflects the dynamics of the scattering centres within the sample. Light propagation and scattering in turbid media can be also described as a diffusion process, in which the

density of photons U is obtained by solving the diffusion equation:

$$\frac{\partial U}{\partial t} = D_{light}\nabla^2 U \tag{1}$$

in which the diffusion coefficient of light is $D_{light} = cl/3$, related to the speed of light c multiplied by mean path length l, defined as the average distance between successive scattering events, assumed isotropic.

In emulsions, the drops are the scattering centres. At first approximation, neglecting near-field and collective effects, the scattering is governed by the Mie law. In this regime, scattering is strongly anisotropic, implying that a sequence of many scattering events is necessary to lose memory of the direction of propagation of light and completely randomize it. Therefore, it is customary to introduce the transport mean free path l^*, defined as:

$$l^* = \frac{l}{1-p} \tag{2}$$

where the persistence parameter $p = \langle cos\theta \rangle$ quantifies the persistence of direction of light propagation after one scattering event, in which light is deflected by the angle θ.

The measured intensity correlation function, g_2, is connected to the electric field correlation function g_1, via the Siegert relation:

$$g_2(t) = A + \beta[g_1(t)]^2 \tag{3}$$

Where A and β are the baseline and the contrast, which depend on several experimental parameters. It is instructive to consider $g_1(t)$ as given by the sum of the contributions from all possible photon path lengths s. Each path includes a number of scattering events roughly proportional to s. This accounts for a different degree of decorrelation of the electric field. This is weighted by the corresponding probability $P_{l^*}(s)$, which in turn depends on the experimental geometry and on the mean free path of transport l^*:

$$g_1(t) = \int_0^\infty P(s|l^*) g_{1,s}(t) ds \tag{4}$$

In this analysis, each $g_{1,s}(t)$ is given by:

$$g_{1,s}(t) = \exp\left(-\frac{s}{3l^*}k_0^2\langle\Delta r^2(t)\rangle\right) = \exp\left(-\frac{1}{3}\frac{s}{l^*}k_0^2\left(6Dt + (v^*t)^2\right)\right) \tag{5}$$

in which k_0 is the light wave-vector in the medium and $\langle\Delta r^2(t)\rangle$ the mean square displacement (MSD) of the scattering centres. The MSD is a combination of diffusive and ballistic dynamics, the former being characterized by the Brownian diffusivity D, the latter by the ballistic velocity v^* representing the average velocity of relative displacement between scattering centres.

In photon correlation spectroscopies where the light propagation and exchanged momentum are known exactly, such as Dynamic Light Scattering (DLS) or X-ray Photon Correlation Spectroscopy (XPCS), the process of deriving the MSD of the scattering centres over time enables analysis of the underlying dynamics [34].

The scenario differs in DWS, particularly in the experiments on emulsions on the ISS, where the value of l^* is not independently known. It depends on drop size and the degree of (de)emulsification. Therefore, it must be determined concurrently with the dynamics. We developed an analysis scheme for DWS applied to emulsion dynamics[26]. To ensure robust analysis, we model the dynamics using as the sum of Brownian and ballistic displacements. We simultaneously determine l^*, D and v^*. We also demonstrate that under 1G conditions, we can obtain both the mean radius and the width of the DSD. This is enabled by accurate determination of the distributions of path lengths $P(s|l^*)$ which we obtain by Monte Carlo simulations that include the experimental geometry, of the shape of the impinging laser, and the collection areas both in transmission and backscattering. In particular, for each value of l^* and the two detectors placed in forward (FW) and backscattering (BS), we simulate path length distributions $P_{FW}(s|l^*)$ and $P_{BS}(s|l^*)$ describing the probability of path length s in a sample characterized by a given value of l^*.

For each pair of correlation functions, a model based on eq. (4) and (5) is fitted for each possible value of l^*. The best fit yields the value of l^* together with the dynamic parameters D and v^*, separating structure and dynamics and distinguishing Brownian and ballistic motions [35–37].

Compared to the standard interpretation scheme for DWS which is based on the analytical solutions for the diffusion of photons in idealized geometry, this approach is more accurate for two reasons:

1) it includes finite sample effects which otherwise mask dynamic features, i.e. the shape of $P(s)$ may induce a more or less steep decay of the correlation function, according to eq.4.

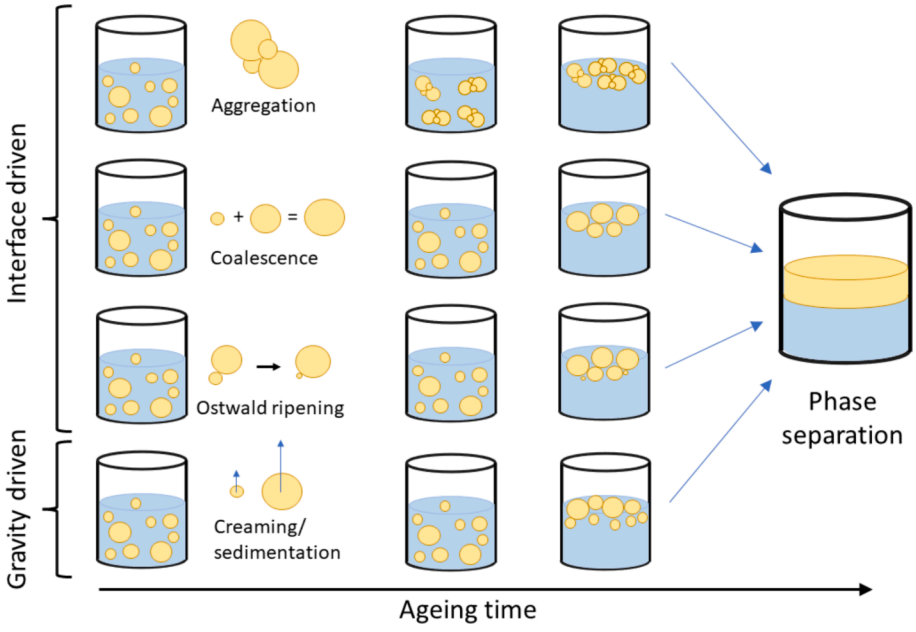

Fig. 1. Primary mechanisms of emulsion ageing, driven by interfacial interactions or by gravity.

2) for sample cells whose size approaches l^*, the discrete nature of the light propagating via successive scattering events is better approximated by a random walk rather than continuous diffusion.

Once D is obtained, the Stokes-Einstein relation yields the drop radius R in case of monodisperse samples:

$$R = \frac{k_B T}{6\pi\eta D} \tag{6}$$

where $k_B T$ is the thermal energy, and η is the viscosity of the continuous phase.

In the general case of a polydisperse DSD, the size-dependent difference in scattering power of the different drops implies that the radius determined by DWS is an average weighted by the different scattering cross sections (as in the case of DLS) but also by the contribution of each size to the light propagation, encoded in l^*. The emulsions in this study can be described as bidisperse, which simplifies the treatment in the Discussion section as well as in the Supplemental Information (SI) section.

The dynamics governing drop motion is important in emulsions in both 1G and microgravity. At long times, drop dynamics are expected to be purely diffusive in nature with possible effects of confinement at the highest volume fractions of dispersed phase. Ballistic motion occurs either as consequence of creaming or sedimentation in 1G conditions or manifest as transient acceleration in microgravity, for reasons detailed below. In either case, the quantification of ballistic motion is critical for the assessment of the mechanisms underpinning emulsion ageing.

2. Materials and methods

2.1. Sample compositions

The emulsions investigated are aqueous dispersions of medium chain triglycerides (MCT oil, Miglyol 812 N, IOI OLEO, Hamburg). High purity water, with resistivity larger than 18 M $\Omega{\cdot}cm$, was produced by a purification system Elix-MilliQ (Millipore, Burlington, MA, USA). Based on the technical sheet provided by the producer, MCT is a mixture triglycerides of saturated vegetable-oil derived fatty acids: mostly capric (41 %) and caprylic (58 %), and minor quantities (<1 %) of shorter and longer chain fatty acids. We investigated emulsions with volume fractions of oil, $\Phi = \frac{V_{oil}}{V_{oil}+V_{water}}$ of 20%, 30% and 50%. For technical reasons, a small but well controlled quantity of air is unavoidably present in all the cells, corresponding to a maximum of 4 % of the total cell volume.

Emulsions are stabilized by non-ionic surfactant 21-ethylene glycol mono *n*-dodecyl ether (C12EO21) CAS 9002–92-0, produced under the commercial name BL-21 by Nikko Chemicals, Japan. In the preparation, it is dissolved in the water phase, and its long hydrophilic head, compared to the alkyl chain warrants a negligible solubility in the oily phase. The surfactant HLB is 19 and the resulting emulsions are, coherently, oil-in-water. The investigated concentrations are $1.0{\cdot}10^{-5}M$ and $4.0{\cdot}10^{-5}M$.

To validate the DWS results and to calibrate some of the optical parameters of the instrument, we used a stable standard calibration sample (NP suspension) was obtained by dispersing carboxylate-modified polystyrene nanoparticles (CLB9, Sigma-Aldrich/Merck) of nominal size $900 \pm 50nm$ in an aqueous phase made by a mixture of D_2O/H_2O matching the density of polystyrene. With a particle concentration of 0.3%w/w we obtained a transport mean free path $l^* = 1.03 \pm 0.03mm$, resembling a typical value for the samples of interest.

2.2. Surfactant characterisation by interfacial tensiometry

The interfacial tension (IT) – concentration isotherm of the C12EO21 aqueous solutions vs. MCT oil has been characterised using a dynamic pendant drop tensiometer (PAT1, Sinterface, Germany). Measured IT values are reported in Fig. 2 together with the best fit curve corresponding to the prediction of a two-state adsorption model.

Previous work shows that that the adsorption features of polyethoxylate surfactants, such as C12EO21 at water–air and water–oil interfaces are well described within a model assuming that the surfactant molecules capable of adsorbing in two distinct states [38]. The model assumes that the hydrophilic moiety can assume different orientations, from nearly parallel to nearly perpendicular to the interface. As the density of adsorbed molecules increases, the interfacial tension decreases.

In the model, the total adsorption $\Gamma = \Gamma_1 + \Gamma_2$ is the sum of the adsorptions Γ_1 and Γ_2 in these states, characterised respectively by given occupation areas ω_1 and ω_2 and surface activities b_1 and b_2. These quantities are linked by the relation $b_1 = b_2(\omega_1/\omega_2)^{\alpha}$, where α is an exponent larger than 1. Given Γ_1 and Γ_2, the interfacial tension, γ, is univocally determined as:

$$\Pi = -\frac{RT}{\omega}\ln(1-\omega\Gamma) \tag{7}$$

where Π is the surface pressure, $\Pi = \gamma_0 - \gamma$, with γ_0 the interfacial tension for the pure water/oil interface, and $\omega = (\omega_1\Gamma_1 + \omega_2\Gamma_2)/(\Gamma_1 + \Gamma_2)$ is the average surface area.

The relation at equilibrium between the bulk surfactant concentration, c, and the interfacial tension, γ, is:

$$b_2 c = \frac{1 - e^{-\frac{\Pi\omega}{RT}}}{\left(\frac{\omega_1}{\omega_2}\right)^{\alpha} e^{-\frac{\Pi\omega_1}{RT}} + e^{-\frac{\Pi\omega_2}{RT}}} \tag{8}$$

Here, the best fit values of the model to the experimental data yields $\omega_1 = 1.4{\cdot}10^{-6}m^2/mol$, $\omega_2 = 2.9{\cdot}10^{-5}m^2/mol$, $b_2 = 26.1m^3/mol$ and $\alpha = 3.8$.

In this study, the concentrations (the arrows in the Fig. 2) are in the submicellar regime, ($CMC = 2.2{\cdot}10^{-4}M$). These were chosen based on 1G experiments that verify that the emulsions switches from marginally stable ($1{\cdot}10^{-5}M$) to stable ($4{\cdot}10^{-5}M$). It is important to note that these concentrations reference the aqueous solution before emulsification. As discussed in the S.I., Section 2, the actual concentrations in the aqueous phase after emulsification are significantly lower (two orders of magnitude) due to the depletion caused by the adsorption to the new drop interfaces created by emulsification.

2.3. Sample cells and emulsification procedure

Microgravity experiments were performed onboard the International Space Station (ISS) in the Soft Matter Dynamics facility (SMD), designed

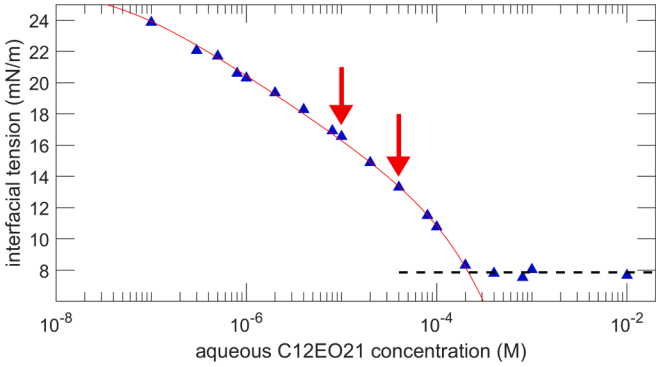

Fig. 2. Interfacial tension-bulk concentration isotherm for C12EO21 at the water/MCT interface. The red line is a fit to eq. 8. Vertical red arrows indicate the concentrations corresponding to the investigated emulsions. (For interpretation of the references to colour in this figure legend, the reader is referred to the web version of this article.)

and built by Airbus under commitment of the European Space Agency. As described previously [39], the primary purpose of SMD is to enable simultaneous DWS and imaging experiments on dispersed turbid samples. In addition to the SMD facility onboard the ISS, a replica termed the Elegant Bread Board (EBB) was also available for ancillary experiments in laboratory. This was used to perform preliminary experiments for the campaign and validating sample formulations and experimental procedures on ground.

Each sample is contained in a sample cell (SC) made by cyclic olefin copolymer, Fig. 3 a). Four sample cells are organized in a sample cell unit (SCU), and a maximum of five SCU are housed in a rotating carousel. The latter allows automated sampling procedures to study emulsions by the different methods of analysis. The volume of the sample cell probed by DWS measures $11 \times 14 \times 11 mm^3$ ($H \times W \times L$). For DWS in transmission, the sample thickness is 11 mm.

Emulsification proceeds by cyclic piston strokes in the sample cell. The piston is driven by a permanent magnet embedded in the piston shaft, which couples to the magnetic field gradients generated by two induction coils. This is powered by a square wave ON-OFF pattern at $18Hz$. The protocol for complete emulsification was defined by preparatory experiments conducted in 1G conditions. It consists of four repetitions of a cycle made of two (2) minutes of piston oscillation, followed by one (1) minute at rest. The rest was introduced to mitigate heating effects. This protocol ensures that all the experiments start with emulsions in the same initial condition, irrespective of previous sample history.

2.4. Initial drop size distribution by microscopy

To characterise the initial drop size distribution in the ISS experiments, a specific device for on-ground measurements was developed to emulate the emulsification process performed on orbit. In this device, drops breakup is accomplished by the periodic up and down movement of a plate, fixed at the tip of a piston, inside a cell triggered by a stepper motor. The gap between the plate and the cell walls is the same as in the sample cells used in microgravity experiments. A detailed description of the experimental device can be found in Chondrou et al. [40]. The emulsification process follows the same protocol described previously.

After the end of the emulsification process, the generated emulsion is drained into a polypropylene tube that contains a highly concentrated solution of surfactant to inhibit drop coalescence. A sample is then taken from the diluted emulsion and placed on a microscope slide with a cover glass. A transmitted light optical microscopy (Axiostar plus, Zeiss) combined with a Canon Powershot A640 video camera are used to obtain high resolution (10 megapixels) images of oil drops. Six microscopy images of each emulsion are analysed with BubbleSEdit, a custom-made software for bubbles/drops detection [41]. In this study, the drops are manually identified for greater accuracy. Each image has a different number of drops. However, in each of the produced emulsions more than 1500 drops are analysed. Typical images processed to estimate drop size probability density functions appear in Fig. 4a-d.

The radius of the measured drops is exported from the software, and the drop size distribution is obtained. The distributions are determined in terms of probability density function (PDF), which implies that the integral of the area under each curve is 100 %.

2.5. Diffusing Wave Spectroscopy experiments on emulsions

For DWS experiments, the SMD facility is equipped with a diode-pumped laser with wavelength 532 nm and output power 200mW (DPL 532, Cobolt AB, SE). Light is collected both in forward (FW) geometry and in backscattering (BS) geometry. In FW geometry, light is collected by a single-mode fibre, coupled to a detector combining a four-quadrant avalanche photodiode and a hardware correlator (ALV- Corrtector, ALV-Laser Vertriebsgesellschaft GmbH, Landen, DE). In BS geometry, a triangular prism engraved on the sample cell wall offers orthogonal interfaces to the entrant and exit light (See Fig. 3, panel a). Laser light impinges on one of the prism faces; the other two faces are dedicated to light collection in BS geometry, which encompasses a fibre-coupled ALV-Corrtector, equivalent to the one employed in FW

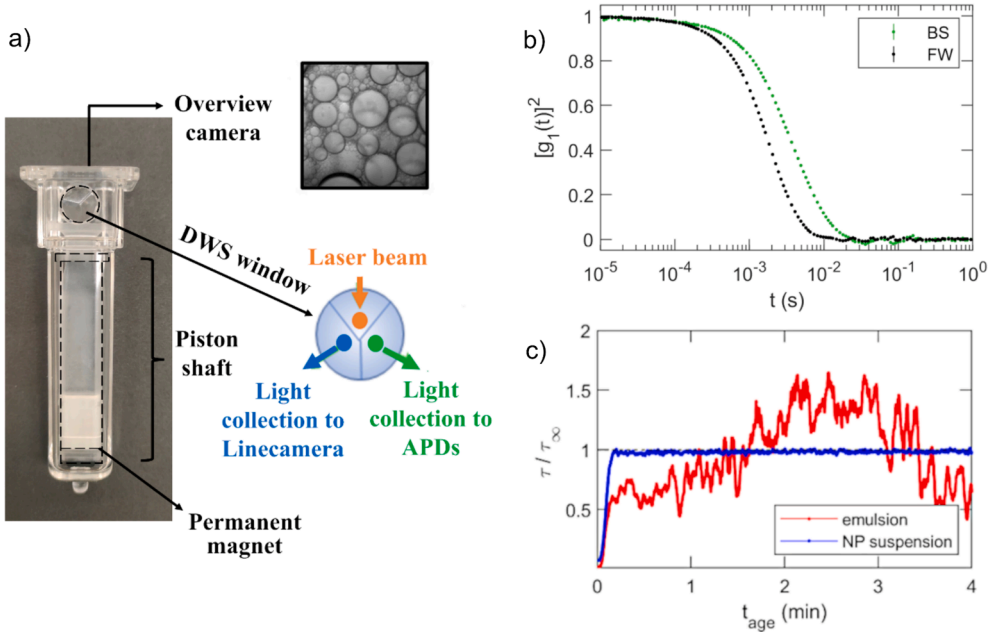

Fig. 3. A: The sample cell. Its top face allows micro-imaging via the overview camera. A triangular prism on the front face (DWS window) offers normal interfaces to the impinging and backscattered (BS) collected light: the three faces correspond to laser entrance (orange dot) and to BS light collection to the APD (green) and to the linecamera (blue). **b:** DWS correlation functions measured in BS (green dots) and in forward (FW, black dots) geometries on an emulsion $[C12EO21] = 1{\cdot}10^{-5}M, \Phi = 20\%$, at $t_{age} = 12min$ after emulsification. **c:** Evolution of DWS decay times in an emulsion ($[C12EO21] = 4{\cdot}10^{-5}M, \Phi = 20\%$, red line) and in the calibration standard (NP suspension, blue line), after they have been subject to the same protocol used for emulsification. (For interpretation of the references to colour in this figure legend, the reader is referred to the web version of this article.)

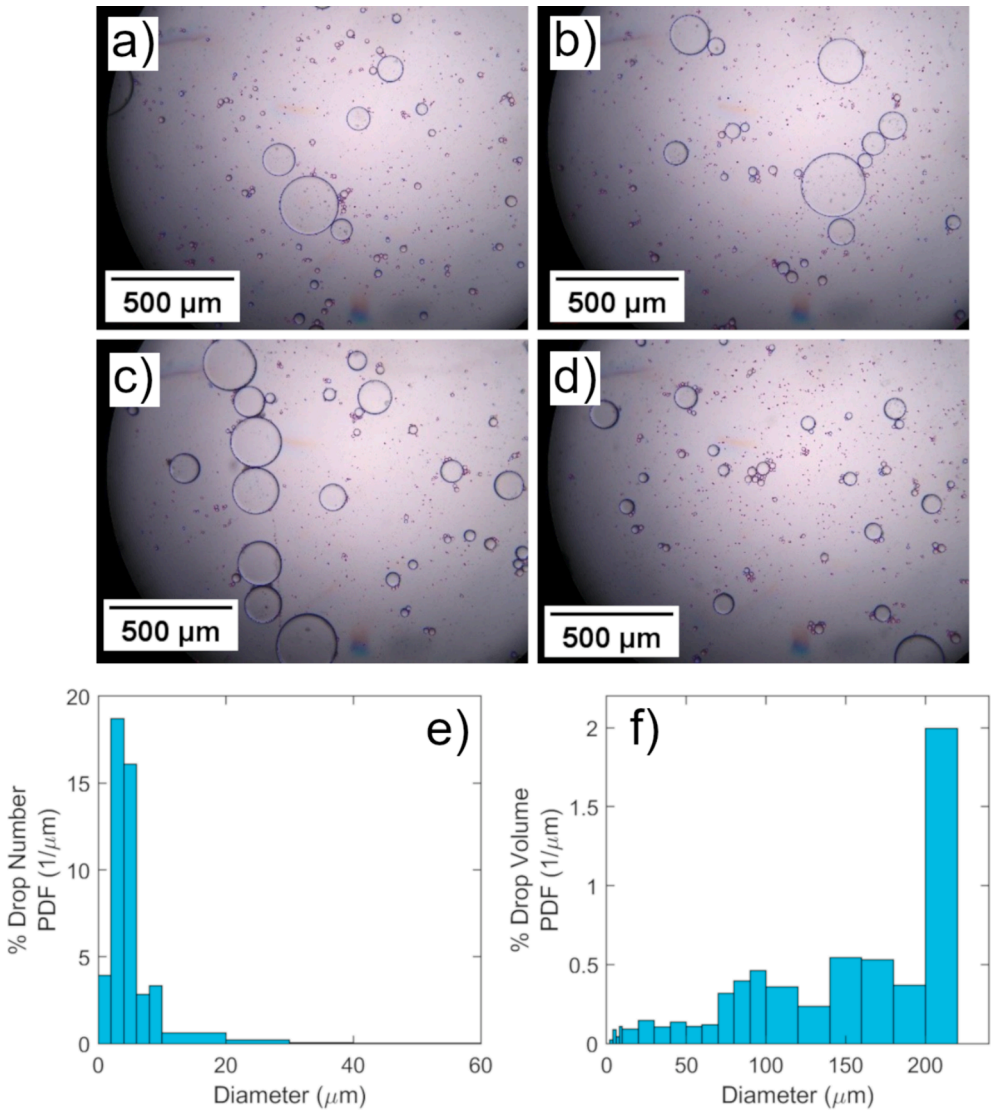

Fig. 4. Panels a-d: Set of microscope images from an emulsion with $[C12EO21] = 4{\cdot}10^{-5}M$ and $\Phi = 30\%$. **Panels e, f**: for the same sample, number probability density function (PDF, e) and volume PDF (f). Note the different axis limits of the two panels.

geometry. Additionally, a high-speed line camera (Basler racer, raL2048-48gm) is coupled with a multi-mode fibre; it can be used for multi-speckle DWS detection.

Rotatable polarizers are included in the fibre collection optics and are used to minimize the contribution of specular reflected light in BS geometry.

A typical experiment on the SMD begins with emulsification of the sample by the protocol described before. Successful emulsification is confirmed by an imaging camera called Overview Camera (OV), equipped with a microscope objective at the top cell window (Pointgrey P/N FL3-GE-50S5M-C, $2448 \times 2048 pixel^2$, field of view $14.4 \times 12.2 mm^2$). Two (2) minutes after emulsification, DWS data are collected: diffused intensity is recorded in FW and BS geometry and CF are calculated sequentially at increasing ages for up to five days. For statistical sampling, CF were integrated from 1 to $5 min$ according to sample age. Only to identify transients, time resolution was increased to 3 secs.

Correlation functions (CF) in FW and BS geometry are computed using a cross-correlation multi-tau scheme, exploiting the four-quadrant geometry of the APD detectors to reach $25 ns$ resolution. The hardware correlator included in the ALV Corrtector itself computes CF up to $102.4 \mu s$. CF at longer lag times are computed via software, using a software correlator provided by Airbus. CF are then indexed and retrieved for further analysis by MATLAB codes developed by us for bulk processing of data.

As described previously, DWS data are interpreted by fitting each CF pair with models based on eq. (4) and (5). Fitting is performed for l^* using a discrete set of candidate values. The fit with the minimum value of the reduced χ^2 is chosen as the best fit. The corresponding values for the fitting parameters diffusivity D and the ballistic velocity v^* are retained. Once the best fit value of l^* is identified, the MSD is extracted by directly by fitting eq. (4) and (5). The sets of $P_{FW}(s|l^*)$ and $P_{BS}(s|l^*)$ used in the fitting were validated by the calibration procedure summarized in the SI.

During an experiment, microgravity conditions may be disrupted for different reasons. For instance, the whole ISS may suddenly accelerate, e.g. due to docking of spacecraft cargos or for orbit manoeuvring. Typically, these motions are predictable, and experiments are planned to avoid them. Occasionally, sudden transients or strong vibrations occur in the SMD due to spurious sources including astronaut activity. To monitor these, thee (3)-axis accelerometers are installed, and their data continuously acquired. We developed a code to automatically exclude DWS datasets affected by any acceleration exceeding a threshold value fixed to $2{\cdot}10^{-3} m/s^2$. In the few cases when severe problems occurred,

the acquisition was repeated.

The temperature of the sample container was kept constant at 20 ± 1 °C, and the temperature of the sample cells were continuously monitored with accuracy better than 0.1 °C.

3. Results

3.1. Initial drop size distribution from microscopy

Typical drop size probability density functions (PDF) immediately after emulsification are reported in Fig. 4 for number density and volume density (e and f, respectively) for an emulsion with $\Phi = 30\%$ and $[\mathrm{C12EO21}] = 4{\cdot}10^{-5}M$. The fact that the size ranges of drop number PDF and drop volume PDF differ by at least an order of magnitude strongly suggests a very broad DSD. In this case, average size and standard deviation of the DSD are not good descriptors of the population, because the distribution is not unimodal. Instead, the bidisperse approximation of the distribution in proposed in [42]. A bidisperse distribution accounts for the experimental observation of drop number and volume PDF located in separated drop size regions and the optimum choice in terms of representing the actual distribution. The bidisperse population is assigned by the quadrature method of moments. If drops are categorized in N classes with diameters $d_i (i = 1, 2 \cdots N)$, the normalized moments of the drop size distribution can be computed as follows:

$$M_k = \frac{\sum_{i=1}^{N} d_i^k}{N} \tag{9}$$

where k is the order of the moments. In particular, the moments with orders $k = 0, 1, 2, 3$ corresponding to drop number, diameter, surface area, volume are employed. The particular range has been chosen based on the number based on the optical drop size analysis technique. A bidisperse distribution with two drop diameters of values d_s (small) and d_L is considered. The number fraction of small and large size is assumed to be w and $1 - w$ respectively. The M_o moment is automatically matched by such a choice. The other three moments are matched by finding proper values for d_s, d_L, w. The resulting equations are:

$$M_1 = w d_s + (1 - w) d_L \tag{10a}$$

$$M_2 = w d_s^2 + (1 - w) d_L^2 \tag{10b}$$

$$M_3 = w d_s^3 + (1 - w) d_L^3 \tag{10c}$$

The above system of three nonlinear equations is solved using a numerical technique for the values of d_s, d_L, w. The number fraction of large drops is $W_L = 1 - w$ and the volume fraction of the small drops is $\Phi_s = w d_s^3 / M_3$. Solving the system of equations (9), (10a), (10b), (10c) yields the results reported in Table 1. The representative diameters of the small drop are also plotted in Fig. 5 c-d.

3.2. Results from Diffusing Wave Spectroscopy

Fig. 3b reports two typical DWS correlation functions for light collected respectively in BS (red points) and FW (black points) geometries. Immediately after emulsification, the dynamics is very fast, also because of residual eddies originated during emulsification. To precisely quantify their duration, the reference sample made of a suspension of nanoparticles was stirred with the same protocol used for emulsification. In this case, no complications arise from coalescence or aggregation of NPs because of the long-time stability. Therefore, we obtain direct quantification of the eddies. Fig. 3c shows the evolution of the relaxation time (blue curve) for DWS in backscattering, normalized to its stationary value measured ten (10) minutes after the end of agitation. We find that eddies are relevant only in the first ten (10) seconds. Interestingly, the same quantity measured on the emulsion shows faster dynamics for at least to two (2) minutes after the end of the agitation (red curve). This is likely because of a richer mechanistic phenomenology beyond simple eddies involving transients in drop interactions. Therefore, we focus our analysis on emulsions in quasi-stationary regime, i.e. starting two (2) minutes after emulsification.

Fig. 5a and b report the ballistic velocity v^* as a function of time for emulsions with surfactant content $[C12EO21] = 1{\cdot}10^{-5}M$ (a), and $4{\cdot}10^{-5}M$ (b) and of different oil volume fractions. The velocity is naturally larger at early times, and it decreases as ageing proceeds. These trends are phenomenologically fitted by exponential decays, indicated by dashed lines. Characteristic times are reported in Table 2. The initial value of v^* is relatively consistent across all samples studied, but in the $\Phi = 50\%$ emulsions, for both surfactant contents, v^* decays significantly faster than in the corresponding emulsions with lower Φ (20% and 30%).

Fig. 5c and d report the mean radius R deduced from DWS diffusivity, for the small drop population of emulsions with surfactant contents $[C12EO21] = 1{\cdot}10^{-5}M$ (panel c), and $4{\cdot}10^{-5}M$(panel d) and of different oil volume fraction, as indicated in the legends. The same figure also reports the initial value of the average drop radius determined by microscopy (data reported also in Table 1, thick lines at early times).

The values of the transport mean free path l^* are reported in panels Fig. 5 e and f for emulsions with surfactant contents (f) $[C12EO21] = 1{\cdot}10^{-5}M$, and (f) $4{\cdot}10^{-5}M$ at different oil volume fractions. In all samples, during the first hours (up to ~ 3 hours) l^* remains nearly constant within the experimental uncertainty. Generally, l^* grows with ageing, although there are large fluctuations and uncertainties that are due to the limited number of drops in the probed volume. In emulsions with $[\mathrm{C12EO21}] = 1{\cdot}10^{-5}M$, both with $\Phi_0 = 20\%$ and $\Phi_0 = 30\%$, l^* grows asymptotically in time. We phenomenologically describe this by a power law.

To deepen the analysis of ballistic motion, in Fig. 6a we report an example of time-resolved measurement of MSD, sampled at three (3) *sec* intervals around the age of 26 min, in an emulsion with $\Phi = 20\%$ and $[\mathrm{C12EO21}] = 1{\cdot}10^{-5}M$. Initially, the MSD (blue lines) grows linearly in time as expected for Brownian diffusion, i.e. with the same slope as the black dashed line. At around nine (9) *sec* (red, orange lines) a transition to super-linear MSD is observed, i.e. with a steeper slope, which is indicative of ballistic contribution to the dynamics. This lasts for a few seconds, and it is followed by the return to the previous diffusive regime (green lines).

An inset Fig. 6a reports the diffusion coefficient D and ballistic velocity v^*. The ballistic velocity is initially negligible and suddenly

Table 1
Drop size distributions from 1G microscopy experiments, obtained by analysis and equations 9 and 10.

[C12EO21]	Φ	Small drop representative diameter $d_s(\mu m)$	Large drop representative diameter $d_L(\mu m)$	% Volume fraction of small drops Φ_s	% Number fraction of large drops W_L	DSD average diameter $\langle d \rangle (\mu m)$
$1.0{\cdot}10^{-5}M$	20%	4.9	125	0.75	0.7	5.8
$4.0{\cdot}10^{-5}M$	20%	6.0	94	1.3	1.9	7.8
$1.0{\cdot}10^{-5}M$	30%	6.8	105	1.8	1.4	8.2
$4.0{\cdot}10^{-5}M$	30%	5.3	128	0.65	1.0	6.6
$1.0{\cdot}10^{-5}M$	50%	6.9	108	0.55	4.4	11.4
$4.0{\cdot}10^{-5}M$	50%	8.4	191	0.35	2.4	12.7

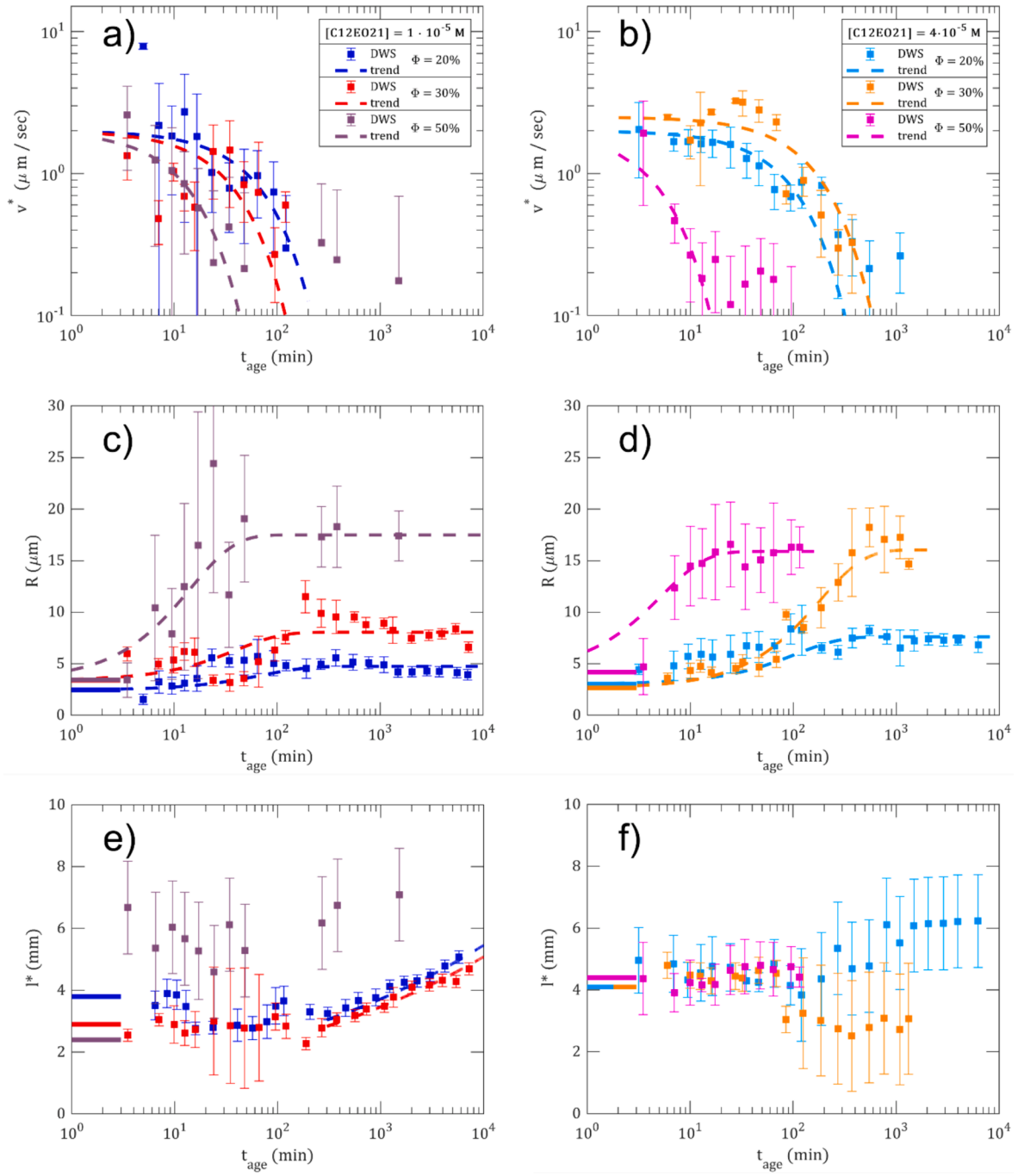

Fig. 5. Evolution of DWS fitted parameters, for emulsions with surfactant contents $1{\cdot}10^{-5}M$ **(panels a, c, e)**, and $4{\cdot}10^{-5}M$ **(b, d, f)** and with different oil fractions (indicated in the legends). **a, b**: ballistic velocities (symbols), and their trends described in the text (dashed lines) **c, d**: mean radii (symbols) for the small drops, and their trends described in the text (dashed lines), compared with the corresponding initial values obtained by microscopy (horizontal lines, see Table 1). **e, f:** l^* (symbols) and their trends (dashed lines), compared with the value estimate by Mie scattering, as described in the text (horizontal lines).

increases to $v^* = 6.8 \pm 0.5 \mu m/s$ for a few seconds, before decreasing back to zero. At the same time, D remains constant within the experimental uncertainty. This demonstrates that ballistic motion happens in transient bursts and is superimposed to Brownian diffusion of drops.

4. Discussion

4.1. Ballistic drop dynamics and coalescence

Drops motion is due to Brownian diffusion and ballistic motion, i.e., displacements at constant velocity (speed and direction). In 1G conditions, creaming or sedimentation induce steady ballistic motion. It was recently shown that from these, it is possible to obtain quantitative information about the 2nd and 4th moments of the drop size distribution [26]. In microgravity, on the contrary, creaming and sedimentation are excluded; nevertheless, ballistic motion is still observed (Fig. 5a,b) with intermittent character (Fig. 6a). This is not to be confused with the dynamics due to the eddies or residual motion caused by the mechanical emulsification process, which dominates only the first tens of seconds as shown in Fig. 3c.

The question is to identify the source of this ballistic intermittent motion. Because of the excellent thermal control of the SMD instrument,

Table 2
Initial ballistic velocity v^*, characteristic time τ_v for its decay, radius of the small drops at initial time R_0 (from microscopy) and its saturation value R_∞ (from DWS).

[C12EO21]	Φ	Initial v^* ($\mu m/s$)	τ_v(min) decay time of v^*	$R_0(\mu m)$	$R_\infty(\mu m)$
$1.0{\cdot}10^{-5}M$	20%	2	$70' \pm 50'$	2.5 ± 0.1	4.7 ± 0.2
$1.0{\cdot}10^{-5}M$	30%	2	$40' \pm 20'$	3.0 ± 0.1	8.0 ± 0.4
$1.0{\cdot}10^{-5}M$	50%	2	$14' \pm 2'$	3.4 ± 0.1	17.0 ± 1.0
$4.0{\cdot}10^{-5}M$	20%	2	$110' \pm 20'$	2.7 ± 0.1	7.6 ± 0.4
$4.0{\cdot}10^{-5}M$	30%	3	$180' \pm 80'$	3.4 ± 0.1	16.0 ± 1.0
$4.0{\cdot}10^{-5}M$	50%	3	$5' \pm 3'$	4.2 ± 0.1	17.0 ± 1.0

we can exclude thermophoretic effects. (In any case, residual temperature gradients would cause a continuous ballistic motion.) The most likely candidate is the occurrence of drop coalescence events.

In $\Phi = 50\%$ emulsions, v^* decays faster for both surfactant contents than for emulsions with lower Φ. We ascribe this difference to de-emulsification occurring in $\Phi = 50\%$ more rapidly, in the first minutes of emulsion life. This interpretation is also supported by the evolution of the drop radius R for the $\Phi = 50\%$ which expands to $R \sim 15\mu m$ more rapidly than in the emulsions with lower oil content. This suggests a major role of the statistical features of drop dynamics. In particular, the probability of drop collision increases with increasing oil content. This may result in an increased number of coalescence events, thus contributing to the rate of de-emulsification.

There are at least two different ways in which coalescence between two drops can induce ballistic motion: either because of 1) velocity fields in the continuous phase in the neighbourhood of the drops that coalesced, with subsequent hydrodynamic correlations and possible displacements of other drops in the nearby, or 2) because of Marangoni-like forces that could originate from surfactant concentration gradients in the continuous phase surrounding the drops that coalesced. This latter mechanism is illustrated in Fig. 6b. This merits further discussion. After the coalescence of two drops, the resulting merged drop has an interfacial area that is smaller than the sum of the individual initial interfaces. For example, in the merging of two drops of the same initial radius R_0, initially the total interfacial area is $8\pi R_0^2$; after coalescence, the final drop has radius $\sqrt[3]{2}R_0$ with a $\sim 21\%$ relative reduction of the area of the interface. This brings out of equilibrium the surfactant adsorbed at the interface, and some of the surfactant will be desorbed to return to equilibrium. This causes a gradient of surfactant concentration in the continuous phase surrounding the volume where the coalescence occurred. Due to Marangoni-like forces, the surfactant-rich region where the coalescence occurred acts as a pit for the surrounding drops, inducing ballistic movements. In addition to intrinsic complexity of the capillary-driven Marangoni motion of a set of droplets, such process is quite complicate to model in a realistic emulsion, due to the competition with the process of surfactant diffusion, which tends to smooth the concentration gradients. This mechanism is however more likely effective in emulsions with surfactant concentrations neither too small nor too large, providing a good compromise between the induced surface tension gradients and the concentration gradients damping by diffusion.

4.2. Evolution of the drop size distribution under ageing

Having identified coalescence as the source of ballistic velocity, its quantification is then related to the mean rate of events in the probed volume, of the order of $(l^*)^3$. As a general trend, in all emulsions the ballistic velocity v^* decays exponentially to zero. The characteristic times τ_v of these decays are reported in Table 2. The detailed mechanism being unknown at present, it is not possible to directly quantify the volumetric rate of coalescence events from the measured ballistic velocity v^*. However, the evolution of ballistic velocity with age is a meaningful indicator of similar evolution of coalescence rates between

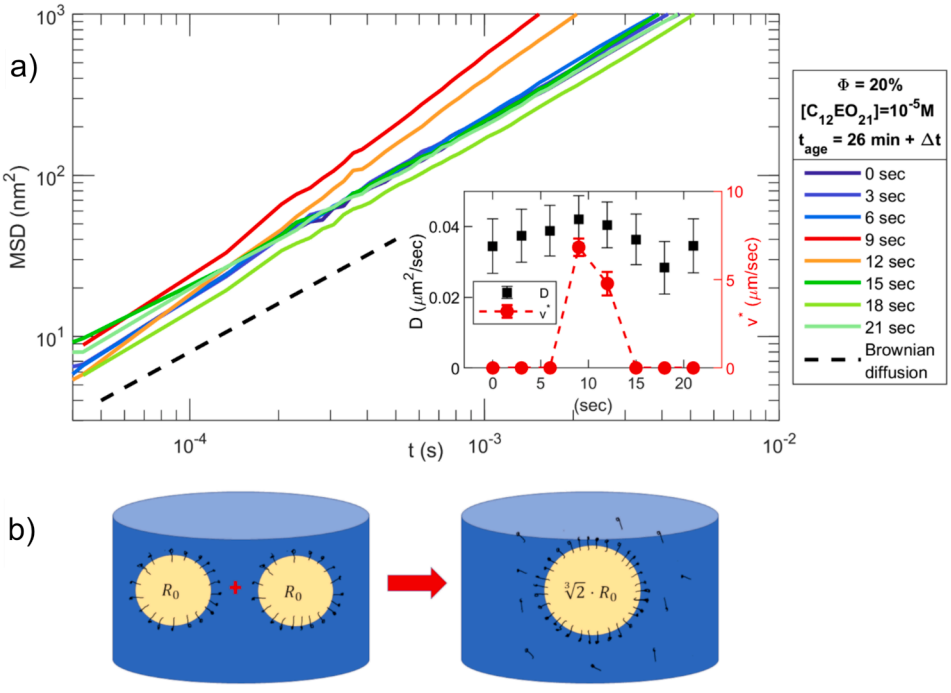

Fig. 6. A: mean square displacement (MSD) in an emulsion with $[C12EO21] = 1{\cdot}10^{-5}M$ and $\Phi = 20\%$ at $t_{age} = 26min$, sampled at different times (coloured solid lines). The dynamic transitions from Brownian (blue lines) to ballistic (red and orange lines), then back to Brownian (green lines). Black dashed line shows for reference the Brownian slope of MSD. **Inset** Diffusion coefficient D (black squares) and ballistic velocity v^*(red dots), obtained from these data. **b:** sketch of the hypothesized effects following drop coalescence: when two equal drops coalesce, the total interface reduces by $\sim 21\%$, causing surfactant desorption and release. This originates a gradient of surfactant concentration in the continuous phase, which could possibly result in Marangoni-like forces acting on surrounding drops. (For interpretation of the references to colour in this figure legend, the reader is referred to the web version of this article.)

drops.

Recalling the observation by microscopy that the initial drop size distribution is bidisperse [42], we can identify three types of drop coalescence events:

1) Between two small drops; or
2) Between one small and one large drop; or
3) Between two large drops.

In case of binary mixtures of small and large particles (a proxy to bidisperse DSD) it is reasonable to assume that the DWS results can be described by an effective transport mean free path l^*_{eff} and an effective relaxation time τ_{eff} [20]. If we indicate with the subscripts A and B the quantities referring to the small and the big drops respectively, we have:

$$l^{*\,-1}_{eff} = l^{*\,-1}_{A} + l^{*\,-1}_{B} \tag{11}$$

where l^*_X ($X = A$ or B) are those of a hypothetical dispersion of the component A (or B) alone in the same medium. Note that l^*_X depends on the volume fraction Φ_X of each component, and of course on its mean radius R_X. At first approximation with Mie theory as demonstrated in SI for non-interacting spheres, for each component X we have:

$$l^*_X \propto \frac{R_X}{\Phi_X} \tag{12}$$

while the effective relaxation time is given by:

$$\tau^{-1}_{eff} = \frac{l^*_{eff}}{l^*_A}\tau^{-1}_A + \frac{l^*_{eff}}{l^*_B}\tau^{-1}_B \tag{13}$$

It is thus evident that the dynamics probed by DWS is mostly dominated by the component with the shortest transport mean free path, which, for reasonable values of volume fractions, can be safely identified with the population of smallest drops. Any populations with R larger than a few tens of microns contributes only marginally to the DWS signal. Since DWS is mostly sensitive to the population of smaller drops, for which it yields information on the coalescence rate, it appears reasonable to attribute the coalescence rate to events involving small drops.

Immediately after emulsification, the mean value of the initial radius of the small drops determined by microscopy is in good agreement with the initial value obtained by DWS. The agreement between these two independent determinations validates our assumption that the DSD measured in 1G is a reasonable proxy for the homologous sample in microgravity.

The evolution with time as determined by DWS can be phenomenological described by an exponential growth from an initial value R_0 to a saturation R_∞:

$$R(t) = R_\infty - (R_\infty - R_0)\cdot e^{-t/\tau} \tag{14}$$

In this relation, only R_∞ is determined by fitting; R_0 is determined by microscopy. The characteristic time τ is assumed to be the same as for the decay of the ballistic velocities.

In principle, drop growth can arise from coalescence or from Ostwald ripening. However, the occurrence of Ostwald ripening is highly unlikely because of the low solubility of MCT oil in water [43] and the relatively large mean drop size which implies that the growth rate is too small to be observed.

On the contrary, drop-drop reversible aggregation and irreversible coalescence processes are all possible. Because the mean drop radius grows on the same time scale that ballistic velocity decays to zero, the correlation between these two quantities is strong. This leads us to hypothesize that in the first hours of ageing, the drop population evolves mainly via coalescence events involving two small drops (events of type 1).

The value of l^* is reported in Fig. 5e,f. It is interesting to compare the DSD from the DWS results and by microscopy. For a bidisperse sample, l^* can be obtained from eq. (11), given the individual contributions from the two components (X = A and B for small and big drops respectively):

$$\frac{1}{l^*_X} = \sigma(R_X)\cdot(1 - \mathrm{p}(R_X))\cdot N(R_X) \tag{15}$$

In which, $\sigma(R_X)$ are the scattering cross sections, $\mathrm{p}(R_X) = < cos\theta >$ are the persistence parameters for Mie scattering from drops of radius R_X, and $N(R_X)$ are the number densities of the same drops.

The estimated values are reported in Fig. 5e,f. The agreement between the estimates for l^*, and for R_0 based on microscopy and by DWS is again an indication of the consistency of the information obtained by these different approaches.

We emphasize that this can be obtained because of the analysis of DWS based on Optical Monte Carlo simulations of random walk, rather than by using an approximate solution to diffusion equation. The simulation mitigates the problem that typically arises when describing light propagation as a diffusion process when l^* becomes comparable to the cell dimensions.

Interestingly, the time evolution of l^* is not the same as that of the radii. l^* is found to remain constant within the experimental uncertainty on the same time scale on which the mean radius grows. This would be an obvious contradiction in a monodisperse sample. The growth of the radius, together with mass conservation, would imply a reduction of number density of drops, and a growth of l^*.

On the contrary, in a polydisperse sample this may happen. The simplest scenario is that of a bidisperse size distribution, consisting of many small drops and some larger ones. In this case, the population evolution happens via coalescence between small drops. The growth of mean radius at constant volume fraction of dispersed phase would result in a sublinear growth of l^*. For instance, doubling the mean radius from 2 to 4 μm would result in an increase only of 50% of l^*. The change of l^* would be probably be even less evident if the real polydispersity would be considered. Thus this is compatible with the proposed mechanism for the evolution of the drop population proceeding via events of type 1.

Interestingly, on much longer time scales, in the samples with the lowest surfactant content and lowest oil content, we find a transition to a completely different regime of evolution of l^*, which lasts at least for five (5) days. In this regime, l^* grows with a phenomenological power law $l^*(t_{age}) \propto t^{\alpha}_{age}$ with $\alpha \sim 1/6$, (dashed lines in Fig. 5e) while the mean radius remains constant. In this regime, the rate of coalescence events is so low that no ballistic velocity can be measured.

We suggest that this regime can be explained assuming that the driving mechanism of evolution is related to events of type 2, namely coalescence of one small drop with one large. This mechanism does not vary the mean radius of small drops, while it reduces their number density, hence l^* grows. It can be argued that this is the case for an emulsion at late stage of de-emulsification.

In summary, in all the samples we observed immediately after emulsification, the mean drop radius grows steadily with time, while the value of l^* shows no appreciable trend, and the ballistic velocity, initially large, decreases with time. At later times, the radius does not increase, but, in emulsions with $[\mathrm{C12EO21}] = 1\cdot10^{-5}M$, and $\Phi = 20\%$ and 30%, l^* starts to increase, with no measurable ballistic velocity. This trend is represented by the thick dashed lines in Fig. 5c,d.

The evolution of drop populations can be rationalized assuming that initially the small drops in their rapid motion, collide with high probability with other small drops (events of type 1) and as a result of these collisions they may either coalesce or aggregate. In either case, aggregation or coalescence, this process leads to an increase of the hydrodynamic radius. However, it is only in the case of coalescence that one can expect ballistic motions. Therefore, based on the observed ballistic dynamics, we identify the growth of radius as the effect of coalescence.

This regime is observed initially in all emulsions. However, as

described previously, in some emulsions a transition is observed to a different regime. This may be explained if the number density of small drops decreases below a certain threshold. In this case, the most important interaction is between one small and one big drop (type 2 events).

4.3. Role of interfacial properties

Interfacial properties are most closely related to coalescence process. In many cases, stable behaviour for emulsions has been observed when the coverage of the drop interface, $\omega\Gamma$ reach a threshold value [44]. Geometrically, $\omega\Gamma$ is the fraction of interfacial area covered by the adsorbed surfactant molecules. During destabilisation, the drop population may evolve and decrease the total drop interfacial area. As such, the coverage increases.

It is important to underscore that during emulsification the dispersed phase is distributed into a large number of small drops resulting in large increase of the water/oil surface. The consequent adsorption of surfactant molecules at the drops interface can result in a significant depletion of the surfactant concentration in the surrounding matrix phase. To account for this phenomenon, it is important to consider that at equilibrium, for a soluble surfactant (such as C12EO21) adsorption and bulk concentration are related by the adsorption isotherm, $c = c(\Gamma)$, that can be therefore calculated combining it with the mass balance for the available surfactant:

$$\begin{cases} A\Gamma + cV_{water} = c_0 V_{water} \\ c = c(\Gamma) \end{cases} \tag{16}$$

Here, the adsorption isotherm is reported in Fig. 2. The details for the calculation of the depleted concentrations assuming a bidisperse drop size distribution are given in SI Section 2 Surface-related effects on emulsion evolution.

According to the results of the calculation, the observed growth of radii for the small drops implies a modest growth of the coverage. This is likely because their volume fraction is very small (order of few percent), so that the evolution of their size does not significantly affect the ratio between the total interfacial area and the volume of the oil drops.

The absolute values of the coverage for the 20% and 30% volume fractions are compatible with interfaces that are stable against coalescence. Concurrently, we observe a limited growth of the average drop size, and ballistic velocities evolving on the same timescale. In contrast for 50% volume fraction, the coverage, (0.2), suggest a less stable emulsion. This is corroborated by the observed relatively large and quick growth of the average radius (as compared with the smaller volume fractions) and the ballistic velocity at shorter times (<200 min). This does not explain the saturation at larger times. At large oil fractions other factors to become relevant, such as the high probability that two drops approaching beyond some critical distance below which they may coalescence.

All samples with surfactant concentration $4{\cdot}10^{-5}M$ have coverages close to saturation. In this case, the emulsion would be anticipated to display limited coalescence. However, the ballistic velocity and the increase of the drop size as shown by DWS analysis indicates coalescence.

It appears therefore that an analysis based exclusively on the coverage and, therefore on an equilibrium quantity, does not capture the features observed in this study. Dynamic and surface-rheology aspects related to the surfactant bulk-interface exchange are also expected to play a role in the stability of the liquid film between approaching and possibly coalescing drops. On the other hand, drop coalescence involves more complicated pathways, depending on drop crowding and drop dynamics, also considering the formation of small aggregates, that are not fully captured by the present DWS analysis and deserve to be further investigated.

5. Conclusions

We performed a comprehensive investigation of oil-in-water emulsions formulated with a non-ionic surfactant, focusing on the evolution of the intrinsic dynamics of the drop population. This was made possible by the long-term microgravity conditions of the International Space Station. This enables separation of different destabilization mechanisms and isolation of intrinsic drop population evolution processes. To the best of our knowledge, it is the first time that an investigation with this scope has been reported.

As a result, we have extended the realm of application of DWS [20–25] as implemented on the ESA Soft Matter Dynamics (SMD) facility [39]. To take full advantage of the DWS technique, we utilized an original interpretation scheme developed by us [26], based on optical Monte Carlo simulations to accurately reproduce the propagation of light in the sample cell. The analysis was also supported by ground-based (1G) characterizations of the initial drop size distribution. We establish that the drop population is initially bidisperse, confirming the validity of a previously established analysis[38,42].

We obtained information on the evolution of mean drop radius and types of drop dynamics, e.g., Brownian diffusion and constant velocity, ballistic, relative displacements. This led us to identify different de-emulsification mechanisms and tentatively assess their relative importance as a function of the properties of the drop population and of the liquid interfaces. In all emulsions investigated, our results indicate that at early stages of the emulsion ageing, the mean drop radius grows, and ballistic displacements are important. We speculate that in this regime the drop population evolves mainly via interaction between small drops. Nevertheless, in the emulsions with a low dispersed fraction and with the lowest surfactant content, a crossover to a different regime is found at later times. In this case, the light transport mean free path l^* increases, the average drop radius does not grow, and ballistic dynamics is not observed. We speculate that in this regime and at late stages of de-emulsification, evolution is dominated by aggregation or coalescence between small and large drops.

Open questions remain: what are the physico-chemical bases of the observed evolution? what triggers the observed crossover? what are the relationships to the existing models describing the role of surfactant type and concentration [45,46]. We anticipate that future experiments at 1G and in microgravity will address these.

Author contributions

L. Liggieri, L. Cristofolini, D. Orsi, V. Lorusso, M. Vaccari, J. K. Ferri, R. McMillin and S. Vincent-Bonnieu contributed to the preparation and implementation of the ISS experiment. D. Orsi, V. Lorusso, M. Vaccari, L. Cristofolini, conceptualized and performed the analysis of the DWS experiments. D. Orsi, V. Lorusso, M. Vaccari, L. Cristofolini, J Ferri and R. McMillin performed the emulsification and DWS experiments on ground. L. Liggieri, F. Ravera and E. Santini measured the interfacial properties and calculated the surfactant coverages. A P. Chondrou, M. Kostoglou, T. Karapantsios characterized the drop size distributions on ground. L. Cristofolini and L. Liggieri wrote the manuscript with contributions from all the authors. J. Ferri prepared final editorial review. All the authors participated in the discussions of the manuscript.

Declaration of competing interest

The authors declare that they have no known competing financial interests or personal relationships that could have appeared to influence the work reported in this paper.

Data availability

Data will be made available on request.

Acknowledgements

We acknowledge financial support from the European Space Agency (ESA) via the contract 4000128643/19/NL/PG "Emulsion Dynamics and Drop Interfaces" (EDDI) as well as the U.S. National Aeronautics and Space Administration (NASA) for awards 80NSSC18K0453 and NNX15AE98G. We are also grateful to ESA for the opportunity to perform experiments on the Soft Matter Dynamics (SMD) instrument, and to all the other partners of the EDDI project for useful discussions, and in particular Nikko Chemicals Co. Japan for supplying the surfactants used in this study. Thanks also to IOI OLEO, Germany for providing the investigated MCT oil. We are grateful to the Belgian User Support and Operations Centre team, in the persons of Denis van Hoof, Yenn Arijs, Kevin Voet for their invaluable help during the International Space Station experiments. We also warmly thank Airbus, Friedrichshafen, Germany in the persons of Olaf Schoele-Schulz and Robert Suetterlin from Low Earth Orbit and Suborbital programs for support with the SMD instrument during the 2022 campaign.

Appendix A. Supplementary data

Supplementary data to this article can be found online at https://doi.org/10.1016/j.jcis.2024.07.205.

References

[1] J.C. Berg, An introduction to interfaces and colloids: the bridge to nanoscience, World Scientific (2009), https://doi.org/10.1142/7579.
[2] J.L. Salager, N. Marquez, A. Graciaa, J. Lachaise, Partitioning of ethoxylated octylphenol surfactants in microemulsion-oil-water systems: influence of temperature and relation between partitioning coefficient and physicochemical formulation, Langmuir 16 (2000), https://doi.org/10.1021/la9905517.
[3] J.M. Aubry, J.F. Ontiveros, J.L. Salager, V. Nardello-Rataj, Use of the normalized hydrophilic-lipophilic-deviation (HLDN) equation for determining the equivalent alkane carbon number (EACN) of oils and the preferred alkane carbon number (PACN) of nonionic surfactants by the fish-tail method (FTM), Adv. Colloid. Interface. Sci 276 (2020), https://doi.org/10.1016/j.cis.2019.102099.
[4] J.N. Israelachvili, D.J. Mitchell, B.W. Ninham, Theory of self-assembly of hydrocarbon amphiphiles into micelles and bilayers, J. Chem. Soc. Faraday. Trans. 2 (72) (1976) 1525, https://doi.org/10.1039/f29767201525.
[5] R. Nagarajan, Molecular packing parameter and surfactant self-assembly: The neglected role of the surfactant tail, Langmuir 18 (2002) 31–38, https://doi.org/10.1021/la010831y.
[6] F. Ravera, K. Dziza, E. Santini, L. Cristofolini, L. Liggieri, Emulsification and emulsion stability: The role of the interfacial properties, Adv. Colloid. Interface. Sci 288 (2021) 102344, https://doi.org/10.1016/J.CIS.2020.102344.
[7] J. Israelachvili, Intermolecular and Surface Forces, Elsevier (2011), https://doi.org/10.1016/C2009-0-21560-1.
[8] D.N. Petsev, N.D. Denkov, P.A. Kralchevsky, Flocculation of Deformable Emulsion Droplets, J. Colloid. Interface. Sci 176 (1995) 201–213, https://doi.org/10.1006/jcis.1995.0023.
[9] D. Langevin, Coalescence in foams and emulsions: Similarities and differences, Curr. Opin. Colloid Interface. Sci. 44 (2019) 23–31, https://doi.org/10.1016/j.cocis.2019.09.001.
[10] P. Taylor, Ostwald ripening in emulsions, Adv. Colloid. Interface. Sci 75 (1998) 107–163, https://doi.org/10.1016/S0001-8686(98)00035-9.
[11] J. Lei, Y. Gao, Y. Ma, K. Zhao, F. Du, Improving the emulsion stability by regulation of dilational rheology properties, Colloids. Surf. A. Physicochem. Eng. Asp 583 (2019) 123906, https://doi.org/10.1016/j.colsurfa.2019.123906.
[12] R. Aveyard, B.P. Binks, J. Esquena, P.D.I. Fletcher, P. Bault, P. Villa, Flocculation transitions of weakly charged oil-in-water emulsions stabilized by different surfactants, Langmuir 18 (2002) 3487–3494, https://doi.org/10.1021/la011723e.
[13] E. Dickinson, Strategies to control and inhibit the flocculation of protein-stabilized oil-in-water emulsions, Food. Hydrocoll 96 (2019) 209–223, https://doi.org/10.1016/j.foodhyd.2019.05.021.
[14] D. Langevin, On the rupture of thin films made from aqueous surfactant solutions, Adv. Colloid. Interface. Sci 275 (2020) 102075, https://doi.org/10.1016/J.CIS.2019.102075.
[15] E. Santini, F. Ravera, M. Ferrari, C. Stubenrauch, A. Makievski, J. Krägel, A surface rheological study of non-ionic surfactants at the water–air interface and the stability of the corresponding thin foam films, Colloids. Surf. A. Physicochem. Eng. Asp 298 (2007) 12–21, https://doi.org/10.1016/j.colsurfa.2006.12.004.
[16] M.B.J. Meinders, T. van Vliet, The role of interfacial rheological properties on Ostwald ripening in emulsions, Adv. Colloid. Interface. Sci 108–109 (2004) 119–126, https://doi.org/10.1016/j.cis.2003.10.005.
[17] J. Weiss, N. Herrmann, D.J. McClements, Ostwald Ripening of Hydrocarbon Emulsion Droplets in Surfactant Solutions, Langmuir 15 (1999) 6652–6657, https://doi.org/10.1021/la981739d.
[18] L. Plassard, A. Mouret, C. Nieto-Draghi, C. Dalmazzone, D. Langevin, J.-F. Argillier, Comparison of methods used to investigate coalescence in emulsions, Langmuir (2024), https://doi.org/10.1021/acs.langmuir.3c02561.
[19] A.C. Ferreira, A. Sullo, S. Winston, I.T. Norton, A.B. Norton-Welch, Influence of Ethanol on Emulsions Stabilized by Low Molecular Weight Surfactants, J. Food. Sci 85 (2020) 28–35, https://doi.org/10.1111/1750-3841.14947.
[20] D.A. Weitz, D.J. Pine, Diffusing-wave spectroscopy, in: W. Brown (Ed.), Dynamic Light Scattering: the Method and Some Applications, Clarendon Press, 1993.
[21] D.A. Weitz, J.X. Zhu, D.J. Durian, H. Gang, D.J. Pine, Diffusing-wave spectroscopy: The technique and some applications, Phys. Scr. T 49B (1993) 610–621, https://doi.org/10.1088/0031-8949/1993/T49B/040.
[22] D.J. Pine, D.A. Weitz, J.X. Zhu, E. Herbolzheimer, Diffusing-wave spectroscopy: dynamic light scattering in the multiple scattering limit, J. Phys. 51 (1990) 2101–2127, https://doi.org/10.1051/jphys:0199000510180210100.
[23] D.J. Pine, D.A. Weitz, P.M. Chaikin, E. Herbolzheimer, Diffusing wave spectroscopy, Phys. Rev. Lett 60 (1988) 1134–1137, https://doi.org/10.1103/PhysRevLett.60.1134.
[24] S. Cohen-Addad, R. Höhler, Bubble dynamics relaxation in aqueous foam probed by multispeckle diffusing-wave spectroscopy, Phys. Rev. Lett 86 (2001) 4700–4703, https://doi.org/10.1103/PhysRevLett.86.4700.
[25] R. Höhler, S. Cohen-Addad, D.J. Durian, Multiple light scattering as a probe of foams and emulsions, Curr. Opin. Colloid Interface. Sci. 19 (2014) 242–252, https://doi.org/10.1016/j.cocis.2014.04.005.
[26] V. Lorusso, D. Orsi, F. Salerni, L. Liggieri, F. Ravera, R. McMillin, J. Ferri, L. Cristofolini, Recent developments in emulsion characterization: Diffusing Wave Spectroscopy beyond average values, Adv. Colloid. Interface. Sci 288 (2021) 102341, https://doi.org/10.1016/j.cis.2020.102341.
[27] N. Galvani, M. Pasquet, A. Mukherjee, A. Requier, S. Cohen-Addad, O. Pitois, R. Höhler, E.I. Rio, A.I. Salonen, D.J. Durian, D. Langevin, Hierarchical bubble size distributions in coarsening wet liquid foams, (2023). Doi: 10.1073/pnas.
[28] M. Pasquet, N. Galvani, A. Requier, S. Cohen-Addad, R. Höhler, O. Pitois, E. Rio, A. Salonen, D. Langevin, Coarsening transitions of wet liquid foams under microgravity conditions, Soft. Matter 19 (2023) 6267–6279, https://doi.org/10.1039/D3SM00535F.
[29] F. Salerni, D. Orsi, E. Santini, L. Liggieri, F. Ravera, L. Cristofolini, Diffusing wave spectroscopy for investigating emulsions: II. Characterization of a paradigmatic oil-in-water emulsion, Colloids. Surf. A. Physicochem. Eng. Asp 580 (2019) 123724, https://doi.org/10.1016/j.colsurfa.2019.123724.
[30] D. Orsi, F. Salerni, E. Macaluso, E. Santini, F. Ravera, L. Liggieri, L. Cristofolini, Diffusing wave spectroscopy for investigating emulsions: I. Instrumental aspects, Colloids. Surf. A. Physicochem. Eng. Asp 580 (2019) 123574, https://doi.org/10.1016/j.colsurfa.2019.123574.
[31] R.E. McMillin, D. Orsi, L. Cristofolini, J.K. Ferri, Particle sizing in non-dilute dispersions using diffusing wave spectroscopy with multiple optical path lengths, Colloids. Interface. Sci. Commun. 49 (2022) 100641, https://doi.org/10.1016/j.colcom.2022.100641.
[32] S. Cohen-Addad, R. Höhler, Rheology of foams and highly concentrated emulsions, Curr. Opin. Colloid Interface. Sci 19 (2014) 536–548, https://doi.org/10.1016/j.cocis.2014.11.003.
[33] R. Carpy, G. Picker, B. Amann, H. Ranebo, S. Vincent-Bonnieu, O. Minster, J. Winter, J. Dettmann, L. Castiglione, R. Höhler, D. Langevin, Foam generation and sample composition optimization for the FOAM-C experiment of the ISS, J. Phys. Conf. Ser 327 (2011) 012025, https://doi.org/10.1088/1742-6596/327/1/012025.
[34] L. Cristofolini, Synchrotron X-ray techniques for the investigation of structures and dynamics in interfacial systems, Curr. Opin. Colloid Interface. Sci. 19 (2014) 228–241, https://doi.org/10.1016/j.cocis.2014.03.006.
[35] X.-L. Wu, D.J. Pine, P.M. Chaikin, J.S. Huang, D.A. Weitz, Diffusing-wave spectroscopy in a shear flow, J. Opt. Soc. Am. B 7 (1990) 15, https://doi.org/10.1364/josab.7.000015.
[36] D. Bicout, G. Maret, Multiple light scattering in Taylor-Couette flow, Physica. A 210 (1994) 87–112, https://doi.org/10.1016/0378-4371(94)00101-4.
[37] D. Bicout, R. Maynard, Diffusing wave spectroscopy in inhomogeneous flows, Physica. A 199 (1993) 387–411, https://doi.org/10.1016/0378-4371(93)90056-A.
[38] V.B. Fainerman, R. Miller, E.V. Aksenenko, Adsorption Behavior of Oxyethylated Alcohols at the Solution/Air Interface, Langmuir 16 (2000) 4196–4201, https://doi.org/10.1021/la991502x.
[39] P. Born, M. Braibanti, L. Cristofolini, S. Cohen-Addad, D.J. Durian, S.U. Egelhaaf, M.A. Escobedo-Sánchez, R. Höhler, T.D. Karapantsios, D. Langevin, L. Liggieri, M. Pasquet, E. Rio, A. Salonen, M. Schröter, M. Sperl, R. Sütterlin, A.B. Zuccolotto-Bernez, Soft matter dynamics: A versatile microgravity platform to study dynamics in soft matter, Rev. Sci. Instrum. 92 (2021), https://doi.org/10.1063/5.0062946.
[40] A.P. Chondrou, S.P. Evgenidis, K.A. Zacharias, M. Kostoglou, T.D. Karapantsios, Development of an Experimental Device for the Assessment of Emulsions Dynamic Behavior and Stability in Micro-gravity, Microgravity. Sci. Technol 35 (2023) 28, https://doi.org/10.1007/s12217-023-10055-y.
[41] X. Zabulis, M. Papara, A. Chatziargyriou, T.D. Karapantsios, Detection of densely dispersed spherical bubbles in digital images based on a template matching technique, Colloids. Surf. A. Physicochem. Eng. Asp 309 (2007) 96–106, https://doi.org/10.1016/j.colsurfa.2007.01.007.
[42] M. Kostoglou, T.D. Karapantsios, Approximation of any particle size distribution employing a Bidisperse one based on moment matching, Colloids Interfaces 8 (2024) 7, https://doi.org/10.3390/colloids8010007.
[43] L.M. Land, P. Li, P.M. Bummer, The influence of water content of triglyceride oils on the solubility of steroids, Pharm. Res 22 (2005) 784–788, https://doi.org/10.1007/s11095-005-2595-6.

[44] K. Dziza, E. Santini, L. Liggieri, E. Jarek, M. Krzan, T. Fischer, F. Ravera, Interfacial properties and emulsification of biocompatible liquid-liquid systems, Coatings 10 (2020), https://doi.org/10.3390/coatings10040397.
[45] S. Tcholakova, N.D. Denkov, T. Banner, Role of surfactant type and concentration for the mean drop size during emulsification in turbulent flow, Langmuir 20 (2004) 7444–7458, https://doi.org/10.1021/la049335a.
[46] B. Petkova, S. Tcholakova, M. Chenkova, K. Golemanov, N. Denkov, D. Thorley, S. Stoyanov, Foamability of aqueous solutions: Role of surfactant type and concentration, Adv. Colloid. Interface. Sci 276 (2020) 102084, https://doi.org/10.1016/j.cis.2019.102084.